



PAPER • OPEN ACCESS

# Synthesis of Fe-doped ZnO/biochar nanocomposites for acid orange 7 photodegradation and antibacterial activity under visible light region

To cite this article: Nguyen Thi Huynh Nhu *et al* 2024 *Mater. Res. Express* 11 055001

View the [article online](#) for updates and enhancements.

You may also like

- [Land Unit Mapping and Evaluation of Land Suitability for Agro – forestry in Thua Thien Hue province – VietNam as an Example](#)  
Nguyen Ngoc Dan, Lei Guo Ping and Le Phuc Chi Lang
- [Visible-light-driven photocatalytic degradation of doxycycline using TiO<sub>2</sub>/g-C<sub>3</sub>N<sub>4</sub>/BIOCHAR catalyst](#)  
Nguyen Van Hung, Bui Thi Minh Nguyet, Nguyen Ngc Bich *et al.*
- [Tunable electronic properties of InSe by biaxial strain: from bulk to single-layer](#)  
Khang D Pham, Vo T T Vi, Doan V Thuan *et al.*

**ECS**  
The  
Electrochemical  
Society  
Advancing solid state &  
electrochemical science & technology

**DISCOVER**  
how sustainability  
intersects with  
electrochemistry & solid  
state science research

# Materials Research Express



## PAPER

# Synthesis of Fe-doped ZnO/biochar nanocomposites for acid orange 7 photodegradation and antibacterial activity under visible light region

### OPEN ACCESS

RECEIVED  
6 February 2024

REVISED  
24 April 2024



ACCEPTED FOR PUBLICATION  
3 May 2024

PUBLISHED  
14 May 2024

Original content from this work may be used under the terms of the [Creative Commons Attribution 4.0 licence](#).

Any further distribution of this work must maintain attribution to the author(s) and the title of the work, journal citation and DOI.



Nguyen Thi Huynh Nhu<sup>1</sup>, Bui Thi Minh Nguyet<sup>1</sup>, Nguyen Ngoc Bich<sup>1</sup>, Dinh Quang Khieu<sup>2,\*</sup>  and Nguyen Van Hung<sup>1,\*</sup> 

<sup>1</sup> Faculty of Natural Sciences, Dong Thap University, Dong Thap, 81000, Vietnam

<sup>2</sup> University of Sciences, Hue University, Hue, 49000, Vietnam

\* Authors to whom any correspondence should be addressed.

E-mail: [nguyenvanhung@dtu.edu.vn](mailto:nguyenvanhung@dtu.edu.vn) and [dqkhieu@hueuni.edu.vn](mailto:dqkhieu@hueuni.edu.vn)

**Keywords:** Fe-doped ZnO, biochar, photodegradation, acid orange-7, Antibacterial activity

## Abstract

In the present study, different molar ratios of Fe-doped ZnO/biochar (FZBC) were synthesized using a coprecipitation method. ZnO nanoparticles with a size of approximately 30 nm were well dispersed on the biochar matrix. The bandgap energy decreases from 3.11 to 3.08 eV as the Fe-ion concentration increases from 1 to 7 mol%. Photocatalytic studies demonstrated that FZBC exhibited photodegradation toward acid orange 7 (AO7). FZBC exhibited a photodegradation efficiency of AO7 at a concentration of 10 mg. L<sup>-1</sup> (93.17%), which was nine times greater than that of pure ZnO (10.30%). Furthermore, the FZBC materials also demonstrated effective inactivation of *E. coli*, with an antibacterial rate reaching 98%. Overall, these materials are expected to be cost-effective and suitable for photocatalytic degradation and antibacterial activities.

## 1. Introduction

In wastewater, various bacterial species, including pathogenic bacteria, are often present and need to be monitored and controlled during wastewater treatment [1]. In most cases, wastewater treatment criteria focus on coliform organisms, including *Escherichia coli* [2]. *Escherichia coli* is a pathogenic microorganism that can cause waterborne diseases such as diarrhea, cystitis, and pyelonephritis [3]. Its presence in the aquatic environment can disrupt the ecological balance and pose a threat to human health even at low concentrations [4]. Antibacterial agents are essential tools for treating bacterial infections. However, the misuse of antibiotics has led to the emergence of antibiotic-resistant bacterial strains. A 2015 report predicted that antibiotic-resistant bacterial infections will cause 10 million deaths annually by 2050 [5]. Therefore, continued research to develop new antibacterial agents through cost-effective and environmentally friendly nanotechnologies is of paramount importance.

In recent decades, environmental pollution caused by organic compounds, such as dyes, has gained widespread attention worldwide [6]. Acid orange 7 (C<sub>16</sub>H<sub>11</sub>N<sub>2</sub>NaO<sub>4</sub>S), also known as Orange II, is an anionic azo dye that is extensively used in industries such as textiles, leather, cosmetics, paper, agriculture, and food [7]. The presence of dyes in wastewater, even at very low concentrations, is highly noticeable and undesirable [8]. Furthermore, due to the complexity and diversity of dyes in wastewater, it is challenging to find a single treatment method that can completely remove all types of dyes [9]. Therefore, the removal of these colored compounds from industrial wastewater is highly important.

As mentioned above, the world is currently facing a shortage of clean water sources due to growing industry and the release of organic compounds directly into the environment. Organic dyes and bacteria are the main agents of water pollution and cannot be degraded or inactivated under common environmental conditions [10, 11]. Therefore, many methods have been applied, such as chemical oxidation, adsorption, and photocatalysis. Among these methods, photocatalysis is a powerful technique for environmental detoxification

and has emerged as a promising solution due to its cost-effectiveness and environmental friendliness [12, 13]. Various metal oxides, such as TiO<sub>2</sub> [14], ZnO [15], CuO [16], WO<sub>3</sub> [17], Fe<sub>2</sub>O<sub>3</sub> [18], and SrTiO<sub>3</sub> [19], are known for their ability to efficiently photocatalyze organic compounds and effectively inactivate bacteria via photocatalytic chemical reactions. Zinc oxide (ZnO), a group II–VI semiconductor material, is often considered one of the most promising photocatalytic agents due to its nontoxic nature and physical stability [20]. It exhibits excellent antibacterial activity owing to its hydrophilicity and high oxidative capacity [15, 20]. However, there are some limitations to photocatalysis associated with this semiconductor, such as low quantum efficiency, photocorrosion, and limited light absorption due to rapid recombination of photogenerated charge carriers [15]. To overcome these limitations, researchers have explored alternative methods to enhance carrier mobility. There are various ways to modify the optical and other properties of metal oxide structures [21]. The introduction of a dopant into the structure is one such method [22]. The doping of transition metal ions into the ZnO crystal lattice is a promising technique for enhancing photocatalytic activity by introducing new energy levels within the bandgap, primarily improving the electron–hole pair separation efficiency by forming electron traps [23]. Among the transition metals, iron (Fe) is preferred as a dopant because its d-orbitals easily overlap with the valence band of ZnO [24]. When Fe is doped onto ZnO nanostructures, improved antibacterial and magnetic properties have been observed [25]. Doping with Fe atoms can also reduce the particle size and increase the number of active catalytic sites, which is highly beneficial for adsorption in photocatalytic reactions [26]. Furthermore, the absorption spectrum redshifts in the wavelength range of 320–800 nm due to Fe doping, which results in strong optical absorption in the visible light region [27], and chemical precipitation arrays of Fe-doped ZnO show quenching or absorbing properties, indicating their antibiotic properties [28]. Additionally, Fe-based nanomaterials were effective for antibacterial effects, and their degradation was found to be faster. Furthermore, the ionic radius of Fe<sup>3+</sup> (0.06 nm) is smaller than that of Zn<sup>2+</sup> (0.074 nm), creating a charge imbalance and thus enhancing photocatalytic and antibacterial activity [29]. It is clear from these reported results that the influence of Fe atoms on the ZnO defect luminescence band in nanostructures strongly depends on the specific defect structure of the sample and on the growth process used [21].

Recently, to overcome the limitations of ZnO, ZnO nanostructures have been incorporated into various carbonaceous substrates, such as graphene, graphene oxide, and carbon nanotubes [30]. However, these substrates are expensive and involve complex synthesis procedures [30]. Therefore, there is a need to develop cost-effective and environmentally friendly materials that can replace these expensive carbon materials for synthesizing carbon-based photocatalytic materials. In recent years, biochar (BC) has garnered significant attention as a carbonaceous support to enhance the photocatalytic performance of metal oxide composites [31]. BC is a stable, cost-effective product containing carbon obtained through the pyrolysis of biomass materials under oxygen-free conditions [32, 33]. BC serves as an excellent carrier or support material for synthesizing metal oxide composite materials due to its high porosity, large surface area, and presence of functional groups on its surface, providing excellent electron conductivity support for photogenerated electron transfer [33, 34]. *Phragmites australis*, commonly known as common reed, grows predominantly around lakes, rivers, and streams [35]. In Vietnam, *Phragmites australis* grows widely year-round in rural areas, especially in wetland regions. This plant is primarily composed of high-quality biomass materials, including cellulose, hemicellulose, and lignin, making it a potential source for synthesizing BC [35]. Chen M used ZnO/biochar nanocomposites derived from jute fibers for efficient and stable photodegradation of methylene blue dye [36]. Alves *et al* reported that ZnO/biochar composites exhibited more effective antibacterial activity than did pure ZnO [37]. Many studies have shown that the physicochemical properties of synthesized biochar depend largely on the type of raw material and the operating parameters (heating rate, temperature, atmospheric conditions, retention time, etc.) used to form biochar [38], thereby affecting the quality of the resulting photocatalytic composite. Therefore, research into biochar-based composites produced from specific raw biomass sources is necessary. To date, studies related to the synthesis of Fe-doped ZnO/*Phragmites australis* stem-derived biochars for the application of both photocatalytic and antibacterial agents have been limited. This study represents the first use of biochar derived from *Phragmites australis* stems as an environmentally friendly carbon support material for the production of Fe-doped ZnO/biochar composite materials with photocatalytic degradation and antibacterial properties. This material exhibits significant potential as a photocatalyst in environmental treatment applications.

## 2. Experiment

### 2.1. Materials

Chemicals such as sodium hydroxide (NaOH, ≥ 99.0%), hydrochloric acid (HCl, 37%), iron(III) nitrate nonahydrate (Fe<sub>9</sub>H<sub>2</sub>O<sub>3</sub>·3HNO<sub>3</sub>, ≤ 100%), acid orange 7 (C<sub>16</sub>H<sub>11</sub>N<sub>2</sub>NaO<sub>4</sub>S, ≥ 85%), potassium iodide (KI, ≥ 99.5%) and potassium bromate (KBrO<sub>3</sub>, 99.8%) were purchased from Merck. Zinc nitrate hexahydrate (Zn

( $\text{NO}_3$ )<sub>2</sub>·6H<sub>2</sub>O, 98%), *tert*-butanol ((CH<sub>3</sub>)<sub>3</sub>COH, tBA, 99.5%) and L-ascorbic acid (C<sub>6</sub>H<sub>8</sub>O<sub>6</sub>, AA, 99%) were obtained from Sigma-Aldrich. Raw *P. australis* biomass (comprising 43.31% cellulose, 30.82% hemicellulose, and 20.37% lignin [39]) was obtained from the Practice Experiment Center (Dong Thap University, Vietnam).

## 2.2. Synthesis of Fe-doped ZnO/biochar

A total of 3.0 grams of raw *P. australis* biomass was placed in a porcelain boat and heated under nitrogen gas saturation conditions at 400 °C for 2 h (heating rate: 3 °C min<sup>-1</sup>). The product obtained after heating was first washed with 1.0 M HCl solution and then rinsed several times with distilled water until the filtrate became neutral. The washed product was dried at 105 °C to a constant weight and then stored in a moisture-proof container, which served as the raw biochar material (abbreviated as BC).

In the next step, 7.437 grams of Zn(NO<sub>3</sub>)<sub>2</sub>·6H<sub>2</sub>O were dissolved in 80 ml of distilled water and stirred for 10 min. Subsequently, Fe(NO<sub>3</sub>)<sub>3</sub>·9H<sub>2</sub>O with Fe/Zn molar ratios of 1, 3, 5, and 7% was added to the above solutions. In each case, 0.50 grams of BC was added to the respective salt mixed solution and stirred for 12 h. Then, 50 ml of 1.0 M NaOH solution was added dropwise to each beaker, and the mixture was hydrolyzed at room temperature for 4 h and allowed to settle for 1 h. The mixture was then filtered and rinsed several times with distilled water until the filtrate became neutral. The washed product was dried at 105 °C for 12 h, ground into fine particles and heated under nitrogen gas saturation conditions at 450 °C (heating rate: 3 °C min<sup>-1</sup>) for 2 h (at this heating temperature, the synthesized composite materials had the highest photodegradation efficiency of AO7), resulting in the Fe-doped ZnO/biochar composite products, denoted FZBC1 to FZBC7, respectively. For comparison, ZnO/biochar (ZBC) and pure ZnO samples were also synthesized under the same conditions as described above in the absence of Fe(NO<sub>3</sub>)<sub>3</sub> and both Fe(NO<sub>3</sub>)<sub>3</sub> and biochar, respectively.

## 2.3. Characterization of materials

X-ray diffraction (XRD) patterns were measured using a Bruker D8 Advance X-ray diffractometer (Bruker, Germany). The scanning angle ( $2\theta$ ) ranged from 10 to 80° with a step size of 0.03°. Transmission electron microscopy (TEM) and scanning electron microscopy (SEM) images were acquired using a JEOL JEM—1010 transmission electron microscope (USA) and an FEI Nova NanoSEM 450 scanning electron microscope (USA), respectively. Elemental analyses were conducted through EDX mapping spectroscopy using a TEAM Apollo XL EDS system (USA). Fourier transform infrared (FT-IR) spectra of the samples were recorded with an IR Affinity-1S spectrophotometer (Shimadzu). UV-Vis-DRS (ultraviolet-visible diffuse reflectance spectroscopy) spectra were obtained using a UV-2600 instrument from Shimadzu. Nitrogen adsorption/desorption isotherms (BETs) were determined using a Quantachrome TriStar 3000 V6.07 A adsorption instrument. Photoluminescence (PL) spectra were obtained with a Horiba Fluorolog 3 FL3-22.

## 2.4. Photocatalytic degradation of AO7

In this study, a beaker containing 200 ml of 10 mg·L<sup>-1</sup> AO7 solution suspension and 0.1 grams of the photocatalyst were placed under a lamp holder. The light source used was a Compact 50 W-220 V lamp (Dien Quang) equipped with a wavelength cutoff filter ( $\lambda \leq 420$  nm,  $d = 77$  mm). Prior to illumination, the solution was stirred in darkness using a magnetic stirrer for 60 min to ensure adsorption equilibrium. After a certain interval, 5.0 ml of the solution was withdrawn and centrifuged to remove the solid photocatalyst. The concentration of AO7 in the supernatant was analyzed by UV-Vis spectrophotometry (Spectro UV-2650, Labomed, USA). The adsorption efficiency of AO7 (A%) was calculated using the following equation [8]:

$$A(\%) = \frac{(C_0 - C_{0e})}{C_0} \times 100 \quad (1)$$

where  $C_0$  (mg·L<sup>-1</sup>) is the initial concentration of AO7, and  $C_{0e}$  (mg·L<sup>-1</sup>) is the concentration of AO7 at sorption equilibrium time  $t$  (min).

The photodegradation efficiency ( $D\%$ ) of the photocatalyst was calculated using expression (2) [40, 41]:

$$D(\%) = \frac{(C_{0e} - C_t)}{C_{0e}} \times 100 \quad (2)$$

where  $C_{0e}$  (mg·L<sup>-1</sup>) and  $C_t$  (mg·L<sup>-1</sup>) are the AO7 concentrations at the sorption equilibrium time and at an irradiation time of  $t$  (min), respectively. According to the Langmuir-Hinshelwood kinetics model, the photocatalytic degradation of AO7 dye can be expressed by the following equation [42]:

$$\ln \frac{C_t}{C_{0e}} = -kt \quad (3)$$

where  $k$  is the *pseudo*-first-order rate constant,  $C_{0e}$  (mg·L<sup>-1</sup>) are the AO7 concentrations at sorption equilibrium.

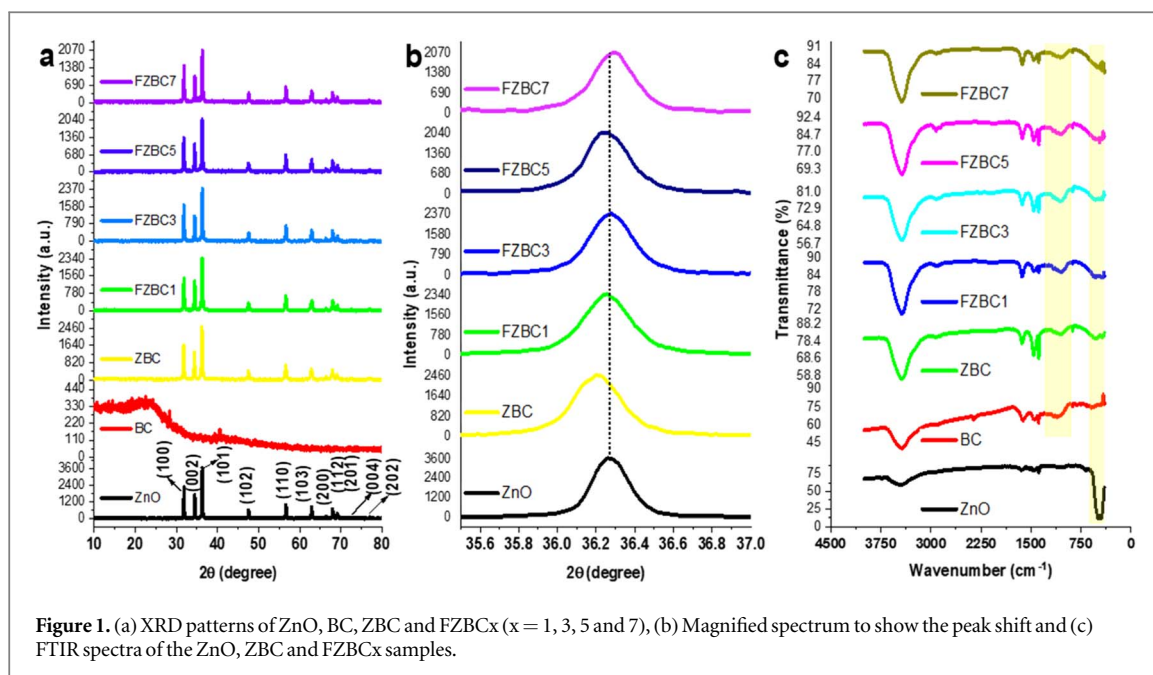


**Figure 1.** (a) XRD patterns of ZnO, BC, ZBC and FZBC<sub>x</sub> ( $x = 1, 3, 5$  and  $7$ ), (b) Magnified spectrum to show the peak shift and (c) FTIR spectra of the ZnO, ZBC and FZBC<sub>x</sub> samples.

## 2.5. Antibacterial activity assessment

The disk diffusion method was employed to assess the antibacterial activity of pure ZnO, ZBC, FZBC1, FZBC3, FZBC5, FZBC7, and pristine EMB (as a control sample). In a typical procedure, 5.0 grams of beef extract and 10.0 grams of peptone were added to a 1000 ml container of distilled water. Subsequently, 100  $\mu\text{l}$  of *E. coli* broth was added to the solution. This mixture was placed in an incubator at 37 °C for 24 h. The *E. coli* broth was diluted to a concentration of 106 CFU  $\text{mL}^{-1}$ , after which 0.05 g of the photocatalyst material was dispersed into 200 ml of this solution. The mixture was stirred for 2 h at 150 rpm under irradiation with a Compact 50 W-220 V lamp. After solidification of the EMB agar, 10  $\mu\text{l}$  of the photocatalytic degradation solution was evenly inoculated onto a Petri dish and placed in a specialized bacterial incubator at 37 °C for 24 h. The number of *E. coli* colonies in the Petri dish was counted using a colony counter. The antibacterial rate ( $\eta\%$ ) was determined using the following formula [43]:

$$\eta(\%) = \frac{Y - X}{Y} \times 100 \quad (4)$$

where Y represents the number of *E. coli* colonies grown on EMB agar and X is the number of *E. coli* colonies grown on agar containing the photocatalyst material.

## 3. Results and discussion

### 3.1. Characterization of photocatalysts

The crystalline structures of the ZnO, BC, ZBC, and FZBC<sub>x</sub> ( $x = 1, 3, 5$ , and  $7$ ) samples were revealed through X-ray diffraction (XRD) (figure 1(a)). The ZnO sample exhibited characteristic diffraction peaks at  $2\theta = 31.7^\circ$ ,  $34.4^\circ$ ,  $36.2^\circ$ ,  $47.5^\circ$ ,  $56.6^\circ$ ,  $62.8^\circ$ ,  $66.4^\circ$ ,  $67.9^\circ$ ,  $69.1^\circ$ ,  $72.6^\circ$  and  $76.9^\circ$ , corresponding to the (100), (002), (101), (102), (110), (103), (200), (112), (201), (004), and (202) crystal planes of the hexagonal wurtzite-phase ZnO structure, respectively (JCPDS card no. 01-075-9743) [20, 36]. The broad peak of biochar at  $2\theta \sim 23^\circ$  was attributed to the characteristic diffraction peak of amorphous carbon [44]. In the ZBC sample and the FZBC samples, characteristic peaks of pure ZnO were also observed, indicating the formation of composites on the biochar substrate. However, no characteristic peak of amorphous carbon was observed in the composite samples. This might be due to the strong overlap of the diffraction peaks of the ZnO hexagonal wurtzite crystal on the characteristic peak of amorphous carbon. Moreover, the peaks of various types of iron oxides or Zn-ferrite were not detected in the diffraction pattern of the FZBC<sub>x</sub> samples, possibly because the amount of Fe impurities was very small compared to the amount of ZnO. Therefore, this small amount of Fe impurity is mostly embedded in the ZnO lattice and cannot be observed because it falls below the detection limit of the instrument. However, figure 1(b) shows that loading ZnO nano particles onto BC has slightly shifted the  $2\theta$  reflection angle of the ZBC sample towards lower values compared to the pure ZnO sample, while the FZBC samples have slightly higher  $2\theta$  values compared to the ZBC sample (table 1), indicating that the presence of Fe impurities tends to slightly increase the  $2\theta$  angle values of ZnO in the FZBC composite. The average crystal sizes



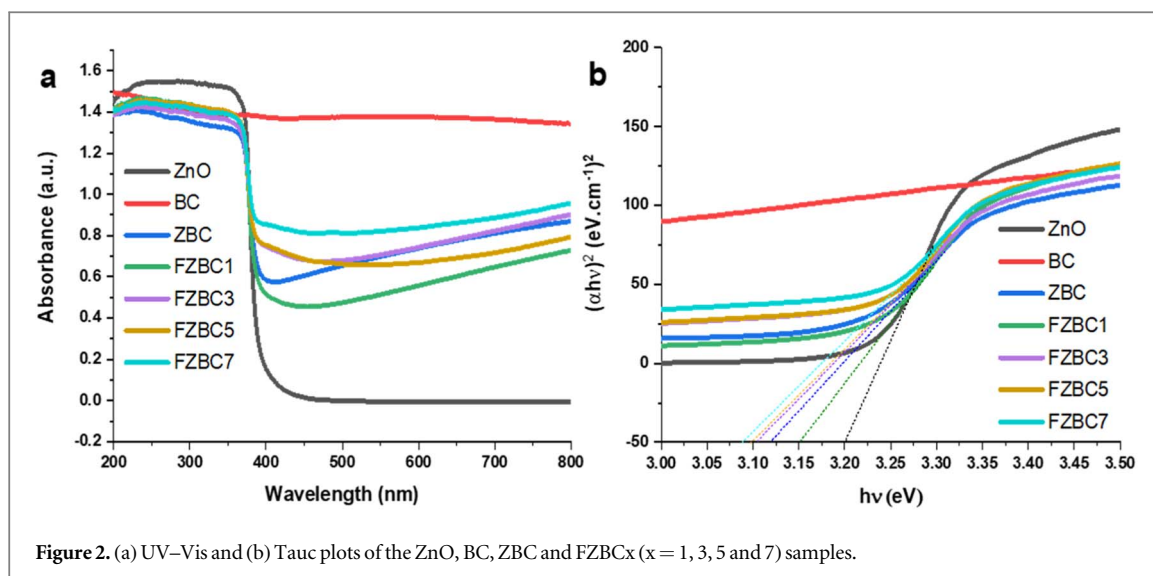


Figure 2. (a) UV-Vis and (b) Tauc plots of the ZnO, BC, ZBC and FZBC $x$  ( $x = 1, 3, 5$  and  $7$ ) samples.

Table 1. The average crystalline size ( $D$ ), reflection angle  $2\theta$  and band gap energy ( $E_g$ ) of the synthesized samples.

Samples	ZnO	ZBC	FZBC1	FZBC3	FZBC5	FZBC7
$D$ (nm)	37.0	28.0	29.0	31.0	31.7	33.2
$2\theta$	36.271	36.204	36.256	36.276	36.254	36.288
$E_g$ (eV)	3.20	3.11	3.15	3.10	3.09	3.08

of the ZnO, ZBC, FZBC1, FZBC3, FZBC5, and FZBC7 samples were calculated using the Scherrer equation for the (101) reflection, yielding values of 37.0 nm, 28.0 nm, 29.0 nm, 31.0 nm, 31.7 nm, and 33.2 nm, respectively (table 1). The variation in particle size indicates that biochar strongly inhibited the crystalline growth of ZnO, while the Fe impurities tended to slightly promote the growth of ZnO crystallites in the ZBC composite within the range of Fe/Zn molar ratios from 1% to 7%.

FTIR was employed to identify the organic and inorganic functional groups present in the samples. Figure 1(c) shows the FTIR spectra of the pure ZnO, BC, ZBC, and FZBC $x$  ( $x = 1, 3, 5$ , and  $7$ ) samples within the wavenumber range of 400–4000  $\text{cm}^{-1}$ . For all the samples, two broad peaks at approximately 3436 and 1635  $\text{cm}^{-1}$  were observed, attributed to the O–H stretching of hydroxyl groups and O–H bending of  $\text{H}_2\text{O}$ , respectively [37]. The peak at 2350  $\text{cm}^{-1}$  is related to C–O stretching in carbon dioxide molecules, which are adsorbed on the sample surface [8, 45]. For the ZnO samples, the peaks at 445  $\text{cm}^{-1}$  and 492  $\text{cm}^{-1}$  are associated with the stretching vibrations of oxygen-metal-oxygen (O–Zn–O) and metal-oxygen (Zn–O) bonds (figure 1(b)) [46], respectively. In the case of biochar, the peaks at 2924  $\text{cm}^{-1}$  and 1619  $\text{cm}^{-1}$  are attributed to the asymmetric stretching of C–H and the  $\text{sp}^2$  character of C=C, respectively [47, 48]. The peak at 1462  $\text{cm}^{-1}$  can be assigned to the carboxylate group ( $-\text{COO}^-$ ) stretching vibration [49]. Peaks in the range between 900  $\text{cm}^{-1}$  and 1300  $\text{cm}^{-1}$  may be related to single C–O bonds, such as those in ethers, and C–OH groups [48]. The peak at 1385  $\text{cm}^{-1}$  is attributed to the vibrational modes of O–H, C–C bending, or C–H bending [50]. In the ZBC composite samples, characteristic peaks of both the ZnO and BC components were observed but with lower intensities; in particular, the vibrational modes of Fe–O and Fe–OH could not be identified in these spectral ranges. This result demonstrates the good substitution ability of  $\text{Fe}^{2+}$  and  $\text{Fe}^{3+}$  ions in the matrix of ZnO [51] and shows the successful formation of ZnO/BC heterojunctions in the ZBC composites [52].

The optical properties of the ZnO, BC, ZBC, and FZBC $x$  ( $x = 1, 3, 5$ , and  $7$ ) samples were assessed via UV-Vis absorption spectroscopy within the range of 200 to 800 nm (figure 2). BC was nearly transparent in the wavelength range longer than 300 nm [53]. Pure ZnO exhibited an optical absorption edge at a wavelength of approximately 387 nm, indicating that its optical absorption ability is primarily in the ultraviolet region [33]. The ZBC sample exhibited an optical absorption edge shifting to approximately 398 nm. Compared to that of pure ZnO, a significant, observable increase in absorption was observed in the visible light range (from 400 to 600 nm) for all FZBC $x$  samples. This suggests that  $\text{Fe}^{3+}$  ions were successfully doped into the ZnO crystal lattice, possibly creating more active defect sites [28, 54]. Moreover, the increased visible light absorption through these defect sites might have led to the enhanced photocatalytic activity of the ZnO crystallites doped in the visible light region. The redshift of the  $\text{Fe}^{3+}$  impurity is due to the  $\text{sp-d}$  exchange interaction between electrons in the

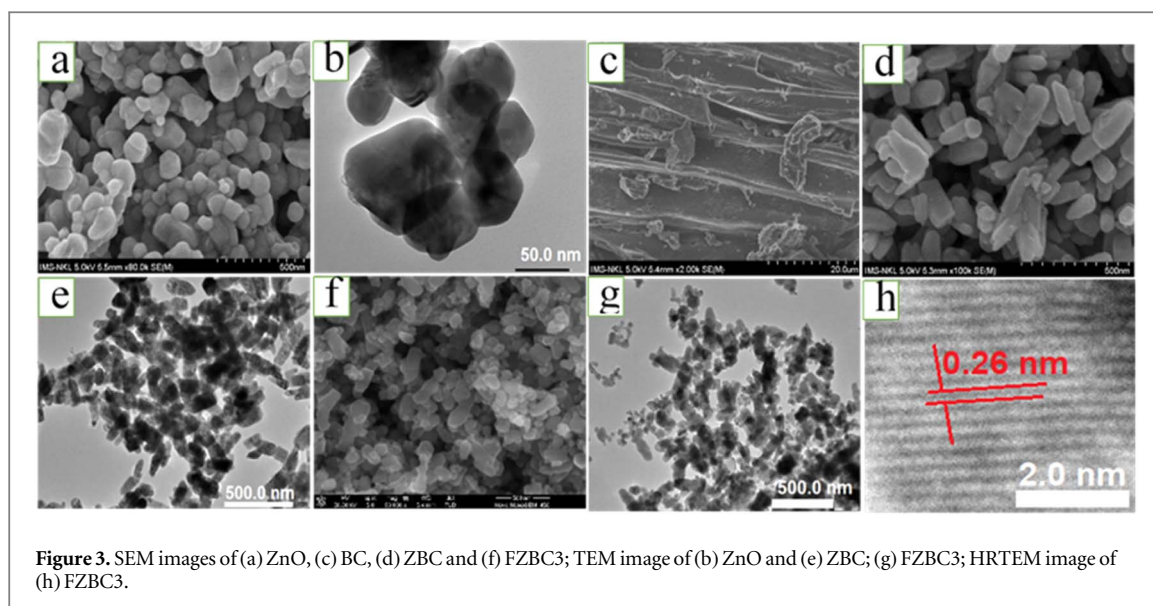


**Figure 3.** SEM images of (a) ZnO, (c) BC, (d) ZBC and (f) FZBC3; TEM image of (b) ZnO and (e) ZBC; (g) FZBC3; HRTEM image of (h) FZBC3.

conduction band of ZnO and the d electrons of  $\text{Fe}^{3+}$  [26]. However, this shift might also be due to the Burstein–Moss effect, which creates additional energy levels for  $\text{Fe}^{3+}/\text{Fe}^{2+}$  below the conduction band of ZnO as the visible light absorption capability increases with increasing amounts of the Fe impurity component [28, 51]. To calculate the band gap values, the Tauc plot relation was used [51]:

$$\alpha h\nu = A(h\nu - E_{bg})^2 \quad (5)$$

where  $\alpha$  is the absorption coefficient,  $h$  is the Planck constant,  $\nu$  is the wavenumber,  $A$  is a constant and  $E_{bg}$  is the energy band gap.

The forbidden energy gap value from the absorption data was calculated by plotting  $(\alpha h\nu)^2$  against the photon energy  $E_{bg} = h\nu$  (figure 2(b)) [51]. The calculated  $E_{bg}$  values for the ZnO, ZBC, FZBC1, FZBC3, FZBC5, and FZBC7 samples were 3.20 eV, 3.11 eV, 3.15 eV, 3.10 eV, 3.09 eV, and 3.08 eV, respectively (figure 2(b) and table 1). These results indicate that Fe doping into the ZnO lattice and its dispersion on the BC support may help narrow the band gap of ZnO in FZBC composites. A decrease in the band gap width, along with an increase in the Fe impurity content, has also been observed in previous research [26, 51, 54, 55].

According to the results of testing the photocatalytic activity of the ZnO, ZBC, and composite samples FZBC1, FZBC3, FZBC5 and FZBC7 (content in section 3.2), we found that the FZBC3 composite achieved the greatest photodegradation performance of AO7 compared to the above samples. Therefore, we focused on analyzing the morphology, elemental composition, photoluminescence and textural properties of sample FZBC3, as presented below.

The morphology and microstructure of the ZnO, BC, ZBC, and FZBC3 samples were observed using SEM and TEM. The ZnO sample (SEM - figure 3(a) and TEM - figure 3(b)) appeared as aggregated spherical particles with an average diameter ranging from approximately 30 nm to 40 nm. Figure 3(c) shows an SEM image of BC in the form of smooth sheets. The ZBC composite sample (SEM - figure 3(d) and TEM - figure 3(e)) comprised both spherical ZnO particles and sheet-like BC, with the ZnO particle size in the ZBC composite ranging from approximately 20 nm to 30 nm, which is smaller than that of pure ZnO. This suggests the inhibitory role of BC in the crystalline growth of ZnO. The FZBC3 sample exhibited large spherical particles (with diameters ranging from 30 to 35 nm) composed of individual smaller nanosized particles that coalesced together and appeared to be successfully attached to the BC surface (SEM—figure 3(f) and TEM—figure 3(g)). The high-resolution TEM (HRTEM) image (figure 3(h)) displayed lattice fringes with a spacing of  $d(002)$  (0.26 nm) characteristic of wurtzite ZnO [56].

EDX- elemental mapping of a selected area on the FZBC3 sample is presented in figure 4. The element Fe was evenly distributed on the surface of BC in the FZBC3 composite (figure 4(d)). In contrast, Zn, O, and C were densely distributed within the FZBC3 network (figures 4(e)–(g)).

The presence of Fe, Zn, O, and C in FZBC3, as well as their integrated images (figure 3(c)), confirms the distribution of these elements in FZBC3. EDX analysis further indicated the presence of Fe, Zn, O, and C in FZBC3 (as depicted in the inset of figure 4(b)). These results demonstrate that Fe-doped ZnO nanostructures were successfully dispersed on BC, indicating that the synthesized FZBC3 composite was free of impurities.

The PL was recorded at room temperature with an excitation wavelength of 368 nm. Figure 5(a) shows that all three samples, namely, ZnO, ZBC and FZBC3, exhibit obvious PL signals with similar curve shapes. The peak

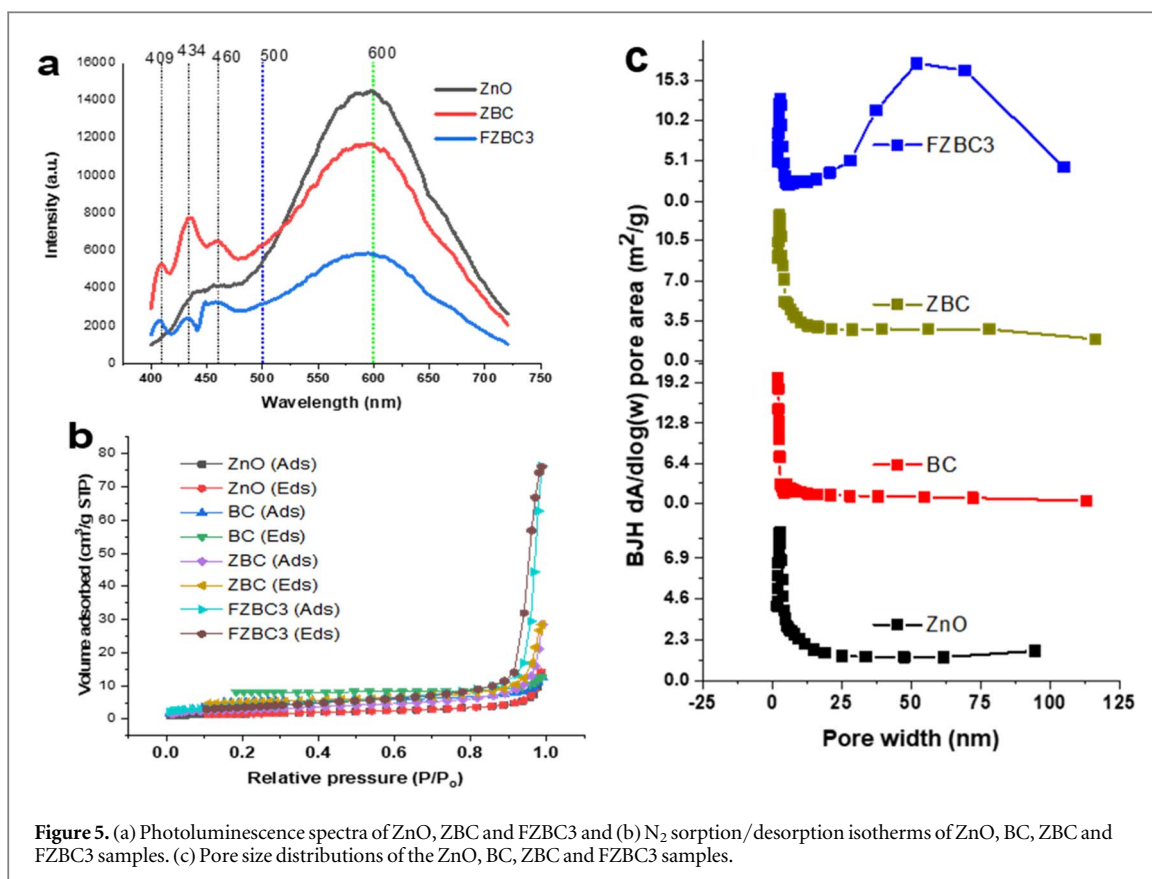
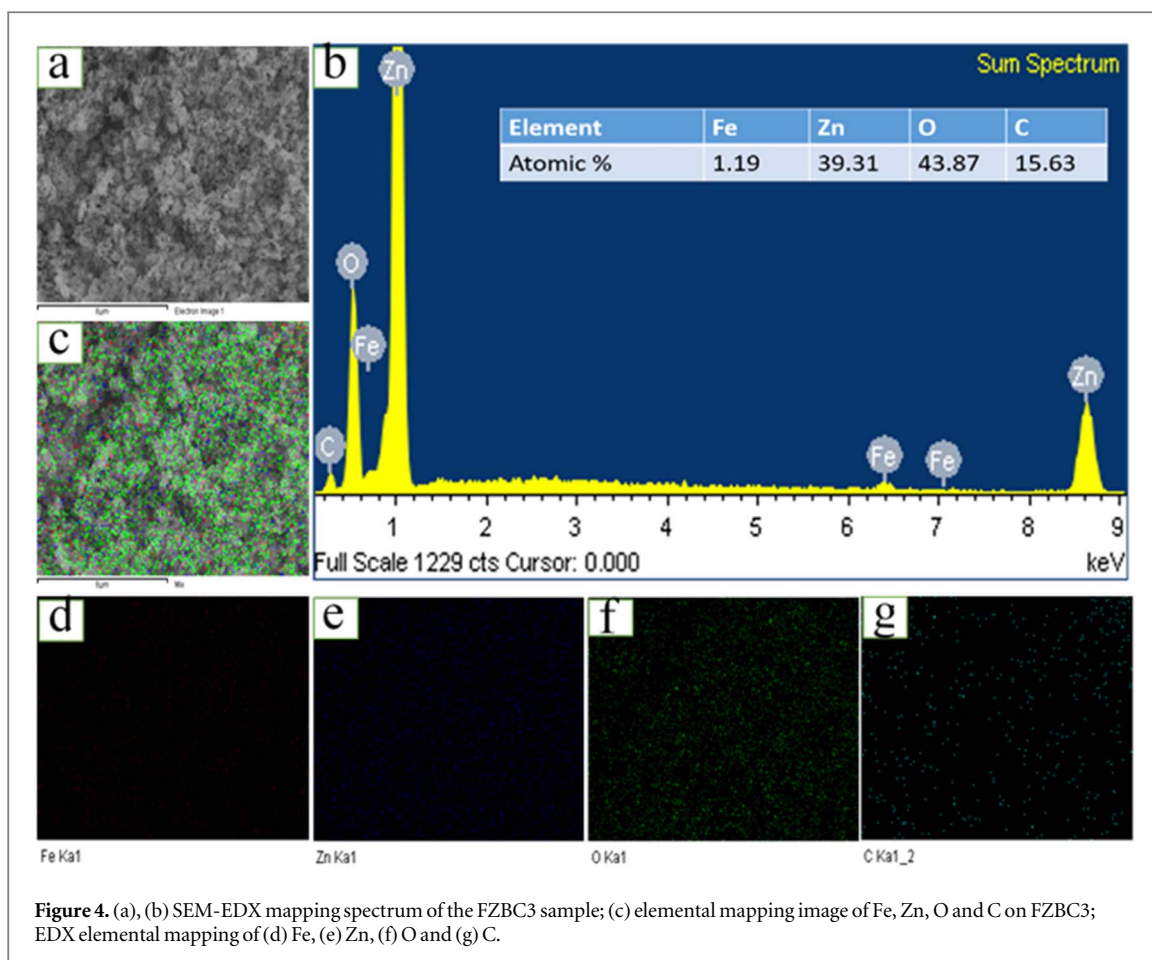




**Table 2.** Textural properties of ZnO, BC, ZBC and FZBC3.

	ZnO	BC	ZBC	FZBC3
Specific surface area ( $\text{m}^2 \cdot \text{g}^{-1}$ )	5.5	22.8	10.3	13.4
Pore volume ( $\text{cm}^3 \cdot \text{g}^{-1}$ )	0.02	0.01	0.04	0.11
Average pore diameter (nm)	16.90	12.43	21.05	35.93

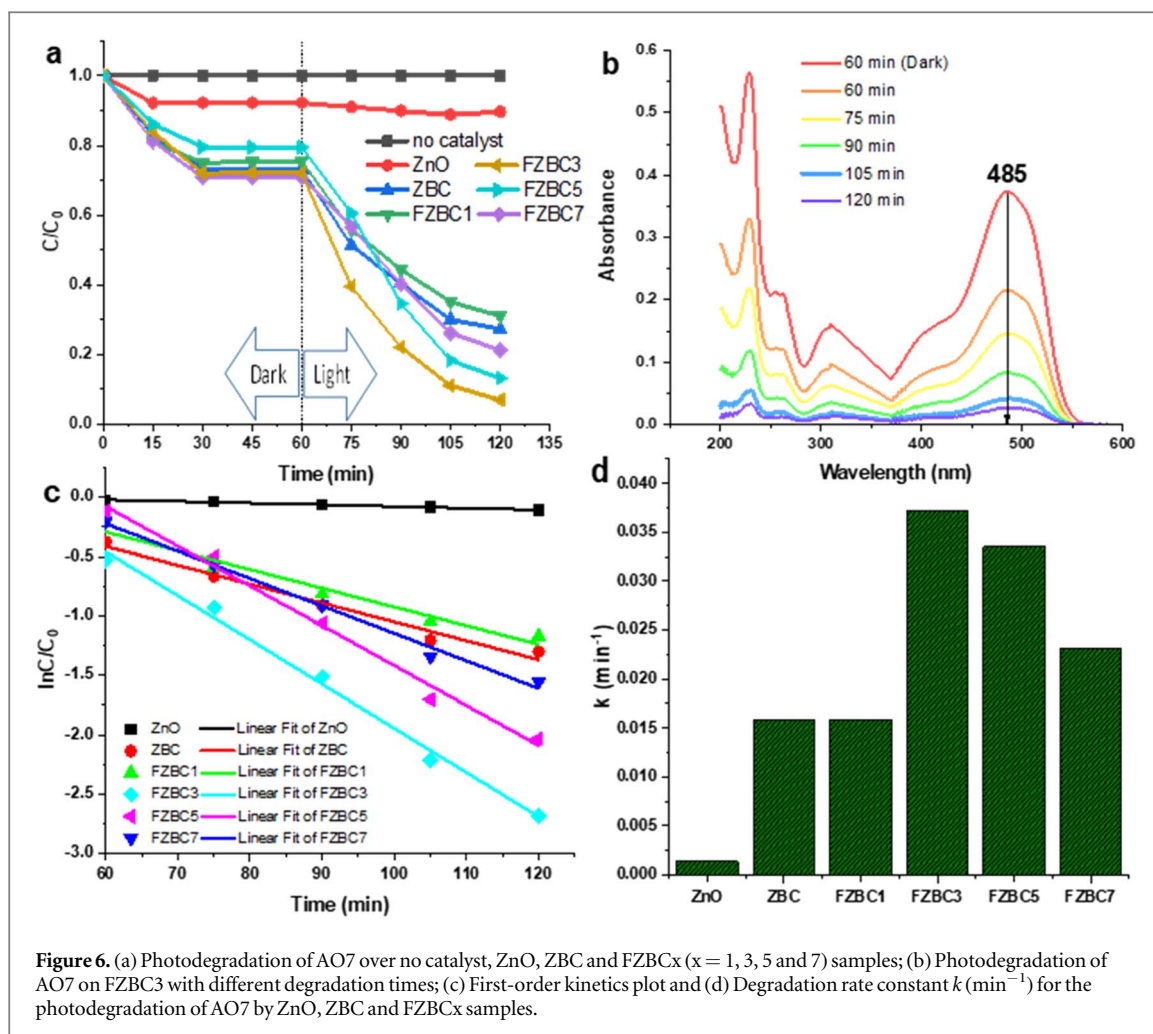
at approximately 409 nm (3.03 eV) corresponds to the transition from the conduction band (CB) to deep holes trapped above the valence band (VB) [57], and the peak at 434 nm ( $\sim 2.85$  eV) is attributed to the electronic transition between the excitonic level and interstitial oxygen ( $\text{O}_i$ ) [58]. The peak at 460 nm ( $\sim 2.70$  eV) corresponds to the direct recombination of a conduction electron in the CB and a hole in the VB [59]. The blue emission peak at 460 nm (2.69 eV) may occur due to the donor-level  $\text{Zn}_i$  to acceptor-level zinc vacancy ( $\text{V}_{\text{Zn}}$ ) [60]. The green emission peak in the range of 500–600 nm (2.48–2.06 eV) is attributed to defects related to oxygen vacancies because of the recombination of photogenerated holes and electrons trapped by singly ionized oxygen vacancies ( $\text{V}_o$ ) [61]. When  $\text{Fe}^{3+}$  ions were incorporated in ZnO and loaded onto a biochar substrate, the fluorescence intensity decreased significantly (figure 5(a)), leading to a decrease in charge carrier recombination, which indicates high electron–hole separation and increased photocatalyst activity.

The porous properties of the ZnO, BC, ZBC, and FZBC3 samples were studied using nitrogen adsorption/desorption isotherms (figure 5(b)). According to the IUPAC classification, the BC sample exhibited type II isotherms with an H3 hysteresis loop, indicating narrow slit-shaped pores [62]. H3 hysteresis is typically observed for nonrigid materials composed of plate-like particles that create slit-shaped pores [63]. The surface characteristics of BC included a relatively high specific surface area and a well-defined pore structure, with a specific surface area of  $22.80 \text{ m}^2/\text{g}$  and an average pore diameter of 12.4 nm (table 2, figure 5(c)). The structural characteristics of BC can provide a good platform for the loading and dispersion of ZnO, and the porous nature of BC is favorable for the formation of active adsorption sites [62]. The ZnO, ZBC, and FZBC3 materials exhibited type IV isotherms with an H4 hysteresis loop, confirming the presence of a mesoporous structure in the prepared materials [64, 65] (see figure 5(c)). The specific surface area, pore volume, and average pore diameter of the ZnO, BC, ZBC, and FZBC3 samples are listed in table 2. The specific surface areas of ZnO, BC, ZBC, and FZBC3 were  $5.5 \text{ m}^2/\text{g}$ ,  $22.8 \text{ m}^2 \cdot \text{g}^{-1}$ ,  $10.3 \text{ m}^2 \cdot \text{g}^{-1}$ , and  $13.4 \text{ m}^2 \cdot \text{g}^{-1}$ , respectively (table 2). The biochar matrix significantly enhanced the specific surface area of ZnO in the ZBC and FZBC3 composites. A larger surface area can provide more active sites. Therefore, the larger BET surface area of the ZBC and FZBC3 composites compared to that of pure ZnO could be one of the reasons for their higher catalytic activity [66]. Furthermore, the formation of a ZnO/biochar heterojunction structure can enhance visible light absorption and efficiently separate photoexcited electron–hole pairs, thus further improving photocatalytic efficiency [67].

### 3.2. Photodegradation of AO7 with different catalysts

The photocatalytic activity of the pure ZnO, ZBC, and FZBC $_x$  ( $x = 1, 3, 5,$  and  $7$ ) samples was studied through experiments involving the degradation of AO7 under visible light irradiation conditions ( $\lambda > 420$  nm), as depicted in figure 6(a). No photocatalytic degradation of AO7 was observed after 2 h of visible light irradiation, indicating that AO7 is stable under visible light irradiation in the absence of a photocatalyst [68, 69]. The ZnO sample exhibited a relatively low AO7 removal efficiency (10.30%) due to adsorption. The composite ZBC showed a significantly greater AO7 degradation efficiency (72.75%) than did pure ZnO, with a 7.06-fold increase. Notably, the FZBC3 composite exhibited the highest photocatalytic efficiency (93.17%) among all the samples, including ZnO (10.30%), ZBC (72.75%), FZBC1 (68.99%), FZBC3 (86.90%), and FZBC7 (78.83%). AO7 degraded 93.17% within 120 min. Figure 6(b) illustrates the gradual degradation of AO7 on FZBC3 over time, with AO7 nearly completely degrading at 120 min. The UV–Vis spectra of the treated AO7 solution are presented in figure 6(b). AO7 possesses four absorption peaks at 229, 260, 311, and 485 nm and a shoulder peak at 407 nm. The peak at 485 nm is attributed to the hydrazone form, whereas the shoulder at 407 nm is attributed to the azo group [70]. In general, the peaks at 229–311 nm correspond to the  $\pi-\pi^*$  transitions in the benzoic and naphthalene rings of AO7, respectively [71]. The decrease in the intensity of these peaks during the reaction indicates the decomposition of the aromatic moieties and color groups of the dye [70, 71].

To gain a better understanding of the reaction kinetics of the process of AO7 degradation, experimental data were fitted using a first-order kinetic model (equation (3)). As shown in the inset in figure 6(c), the photocatalytic degradation curves in all cases were well fitted to the first-order apparent kinetic model. Furthermore, significant differences in photocatalytic activity were observed for ZnO, ZBC, and FZBC $_x$  (figure 6(c)), implying that the combination of ZnO with BC or the combination of Fe-doped ZnO with BC significantly enhanced the photocatalytic activity of ZnO in the composites. Figure 6(d) shows that FZBC3 exhibited the highest degradation rate constant. The rate constant values for ZnO, ZBC, FZBC1, FZBC3, FZBC5, and FZBC7 were



approximately 0.0014 min, 0.0159 min, 0.0158 min, 0.0372 min, 0.0335 min, and 0.0231 min, respectively. A comparison of the apparent first-order rate constants of the FZBC3 catalyst with those in previously published literature, as listed in table 3, reveals that the catalytic activity of the FZBC3 composite is relatively high compared to that in previous reports.

### 3.3. The influence of scavengers

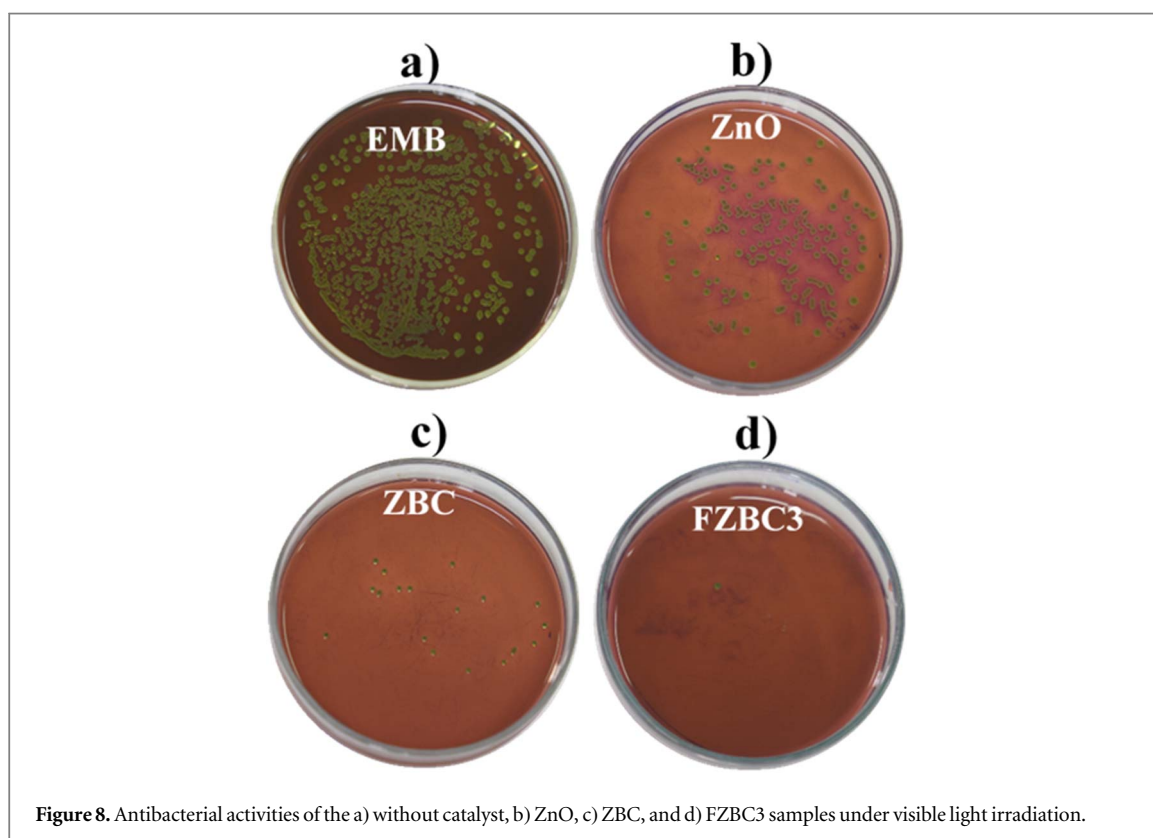
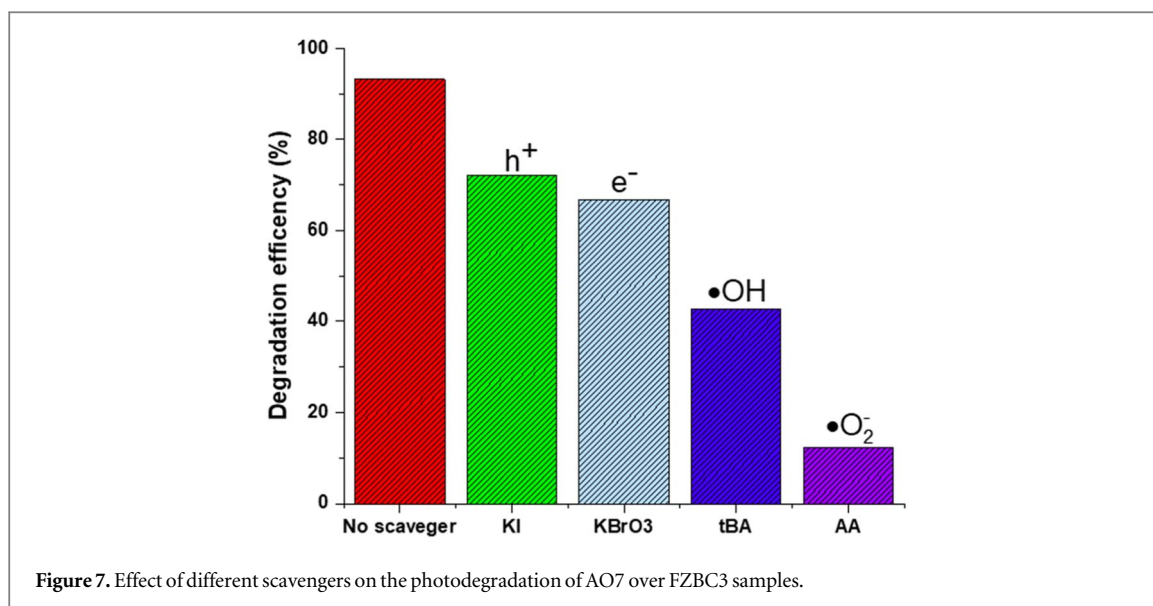
As the photocatalytic process primarily involves the formation of electron–hole pairs ( $e-h^+$ ), superoxide anion radicals ( $\bullet O_2^-$ ), and hydroxyl radicals ( $\bullet OH$ ), it is essential to investigate the activities related to the degradation of AO7 molecules (figure 7). To study these activities related to the photocatalytic process, radical trapping experiments were performed using the FZBC3 catalyst. For this experiment, 10 mM potassium iodide (KI), potassium bromates ( $KBrO_3$ ), tert-butanol (tBA), and ascorbic acid (AA) were added to the DC solution as scavenging agents to capture holes ( $h^+$ ) [76], electrons ( $e^-$ ) [76], hydroxyl radicals ( $\bullet OH$ ) [77], and superoxide radicals  $\bullet O_2^-$  [78], respectively. First, the addition of AA significantly reduced the degradation efficiency to 80.92%, indicating its ability to inhibit  $\bullet O_2^-$  radical formation. Next, the addition of tBA reduced the degradation efficiency to 50.42%, suggesting that tBA interferes with  $\bullet OH$  radical formation. Third, the addition of  $KBrO_3$ , a radical scavenger, reduced the degradation efficiency to 26.46%, indicating that the inhibition of electron formation was not significant. Finally, photogenerated holes  $h^+$  reduced the degradation efficiency to 20.99%, indicating that  $h^+$  is a secondary active species involved in the process. Hence, it is concluded that the formation of superoxide anion radicals  $\bullet O_2^-$  and hydroxyl radicals  $\bullet OH$  in the reaction solution plays a primary role in the AO7 degradation process. These two free radicals possess high reactivity, leading to significant antibacterial activity as well [3, 25].

### 3.4. Antibacterial properties

The antibacterial capacities of pure ZnO, ZBC and FZBC3 were evaluated against *E. coli* (figure 8). Initially, the number of *E. coli* colonies was counted using a bacterial colony counter, and then the antibacterial ratio was calculated using equation (4). ZnO exhibited poor antibacterial properties, achieving an antibacterial ratio of

**Table 3.** Comparison of the rate constant of the present catalyst with the literature values for AO7 degradation.

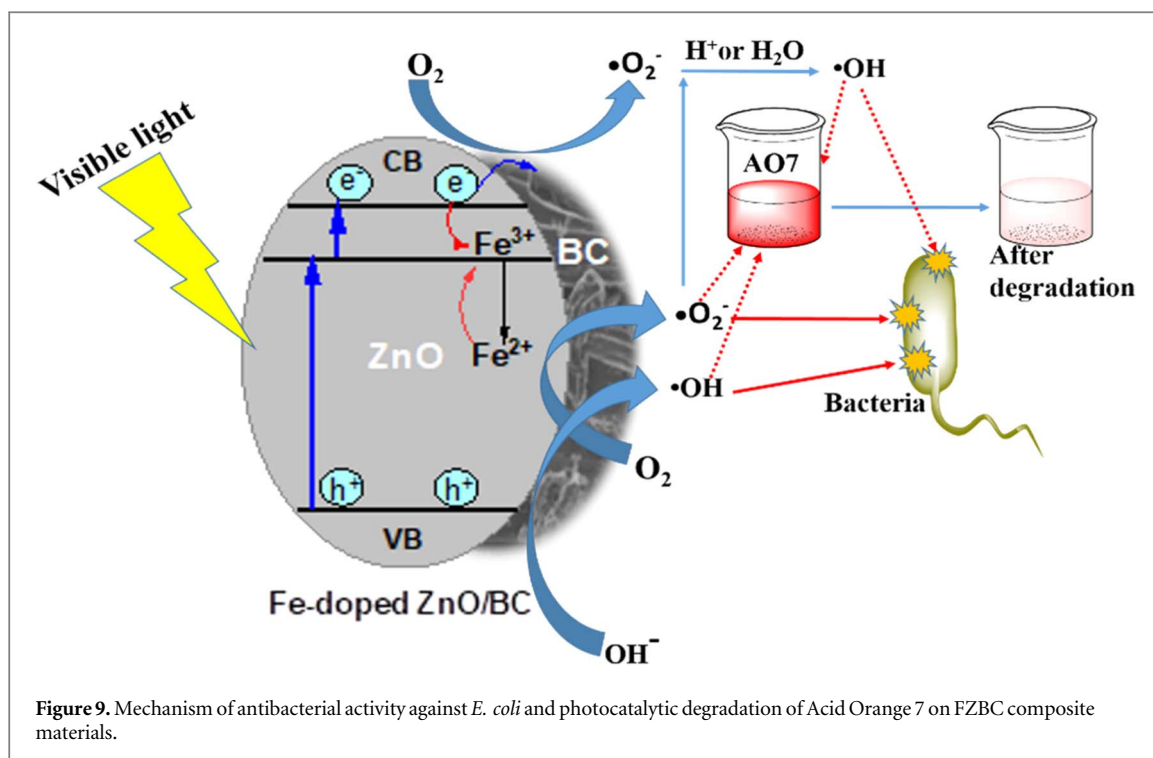
Catalyst	Light source	$C_0$ (mg L <sup>-1</sup> )/Vol. (mL)/ $m_{\text{catalyst}}$ (mg)	$k$ (min <sup>-1</sup> )	References
Fe-doped ZnO/biochar	50 W Compact lamp (filter > 420 nm)	10/200/100	0.0372	The present work
BiOBr(95)-NiO(5)	Haloline ECO400W 230VR7S, OSRAM lamp ( $\lambda \geq 365$ nm)	20/100/100	0.0337	[41]
Ni <sub>3</sub> V <sub>2</sub> O <sub>8</sub> /BiVO <sub>4</sub>	Three 250 W tungsten halogen lamps	17.5/75/75	0.0338	[42]
TiO <sub>2</sub> wrapped graphene	Solar system	10/50/10	0.0451	[72]
Co/N/Er <sup>3+</sup> :Y <sub>3</sub> Al <sub>5</sub> O <sub>12</sub> /TiO <sub>2</sub>	Sun light source	50/1000/2000	0.0369	[73]
Persulfate activated with CuFe <sub>2</sub> O <sub>4</sub> @RSDBC	Visible light illumination	20/100/600	0.0310	[74]
Fe <sup>3+</sup> -doped TiO <sub>2</sub>	400 W medium pressure mercury UV lamp	50/2500/100	0.0451	[75]



only 28.00% (figure 8(b)). This could be attributed to the lack of effective antibacterial agents in the ZnO system. The antibacterial ratio of ZBC against *E. coli* was 81.25% (figure 8(c)). Upon the addition of Fe, the antibacterial ratio of FZBC3 against *E. coli* reached 98.00% (figure 8(d)). FZBC3 exhibited antibacterial ratios greater than 70% and 16.75% greater than those of pure ZnO and ZBC, respectively. This could be because FZBC3 has a greater surface area and larger pore size than ZnO and ZBC (table 2), resulting in better adsorption performance of the FZBC3 composite. Additionally, FZBC3, which has a large surface area, provides more active sites for adsorption and photocatalytic reactions, leading to excellent photocatalytic antibacterial properties [67].

Based on the above experimental results, the photocatalytic AO7 degradation and antibacterial mechanism for the Fe-doped ZnO/biochar (FZBC) catalyst under visible light irradiation can be proposed, as shown in figure 9. When ZnO was doped with Fe<sup>3+</sup> ions, new localized energy levels of Fe appeared in the band gap of ZnO. When FZBC is irradiated, photoinduced electron–hole ( $e^-/h^+$ ) pairs are created, and electrons rapidly move from the valence band (VB) of ZnO to local Fe energy levels along with d-d transitions at the energy level of





Fe doping [26]. These photoexcited electrons are trapped in the Fe energy levels, while the holes remain in the valence band (VB) of ZnO. Electrons from the CB and holes from the VB of ZnO are transferred to the catalyst surface and then consumed in the production of superoxide and hydroxyl radicals ( $\cdot\text{O}_2^-$ ,  $\cdot\text{OH}$ ) by reacting with  $\text{O}_2$ , and  $\text{H}_2\text{O}$  is adsorbed on the FZBC surface. The generated reactive oxygen species attack bacteria and kill them by rupturing their cell walls [75]. The  $\text{h}^+$  hole in the VB of ZnO can directly attack bacteria and decompose AO7 [76]. On the other hand, it can be said that  $\text{Fe}^{3+}$  ions increase the ability to capture electrons, improving the photocatalytic performance under visible light for pure ZnO. Indeed,  $\text{Fe}^{3+}$  ions can trap electrons and be converted to  $\text{Fe}^{2+}$ . Because  $\text{Fe}^{2+}$  is unstable, it can react with oxygen, turning back into  $\text{Fe}^{3+}$  and reducing  $\text{O}_2$  to the superoxide anion radical  $\cdot\text{O}_2^-$  [76]. Overall, the process described above reflects the absorption of more photons under visible light, effectively enhancing the separation of photogenerated electron–hole pairs and generating electrons much more efficiently (figure 9).

#### 4. Conclusions

The Fe-doped ZnO/biochar composite was coprecipitated with *Phragmites australis* stem biomass-derived biochar. The Fe/ZnO nanoparticles and their dispersion on the biochar matrix shifted its light absorption to the visible-light region, resulting in visible-light-driven photodegradation of both the AO7 dye and photodeactivation of *E. coli*. The Fe-doped ZnO/biochar exhibited much greater photocatalytic activity toward AO7 dyes as well as deactivation of *E. coli*. than those of the individual components. These results suggest that the Fe-ZnO/biochar photocatalyst can be considered a method for the treatment of dye-polluted wastewater and that the photocatalytic antibacterial process using this catalyst will be highly useful for systems with high requirements for cleanliness and surface sterility.

#### Data availability statement

The data that support the findings of this study are available upon reasonable request from the authors.

#### Funding

This research is supported by the project SPD2021.01.41.

## Conflicts of interest

There are no conflicts to declare.

## Availability of data and material

The datasets generated during the current study are available from the corresponding author upon reasonable request.

## ORCID iDs

Dinh Quang Khieu  <https://orcid.org/0000-0003-3473-6377>

Nguyen Van Hung  <https://orcid.org/0000-0002-7184-0715>

## References

- [1] Yesilay G, Dos Santos O A L, Bevin Roger A, Hazeem L J, Backx B P, Judith Vijaya J, Kamel A H and Bououdina M 2023 Impact of pathogenic bacterial communities present in wastewater on aquatic organisms: application of nanomaterials for the removal of these pathogens *Aquat. Toxicol.* **261** 106620
- [2] Werkneh A A and Islam M A 2023 Post-treatment disinfection technologies for sustainable removal of antibiotic residues and antimicrobial resistance bacteria from hospital wastewater *Heliyon* **9** e15360
- [3] Guan D L, Niu C G, Wen X J, Guo H, Deng C H and Zeng G M 2018 Enhanced *Escherichia coli* inactivation and oxytetracycline hydrochloride degradation by a Z-scheme silver iodide decorated bismuth vanadate nanocomposite under visible light irradiation *J. Colloid Interface Sci.* **512** 272–81
- [4] Ballesteros-Monrreal M G, Mendez-Pfeiffer P, Barrios-Villa E, Arenas-Hernandez M M P, Enciso-Martinez Y, Sepulveda-Moreno C O, Bolado-Martinez E and Valencia D 2023 Uropathogenic *Escherichia coli* in Mexico, an overview of virulence and resistance determinants: systematic review and meta-analysis *Arch. Med. Res.* **54** 247–60
- [5] Xuan J, Feng W, Wang J, Wang R, Zhang B, Bo L, Chen Z S, Yang H and Sun L 2023 Antimicrobial peptides for combating drug-resistant bacterial infections *Drug Resist Updat* **68** 100954
- [6] Al-Tohamy R, Ali S S, Li F, Okasha K M, Mahmoud Y A, Elsamahy T, Jiao H, Fu Y and Sun J 2022 A critical review on the treatment of dye-containing wastewater: Ecotoxicological and health concerns of textile dyes and possible remediation approaches for environmental safety *Ecotoxicol. Environ. Saf.* **231** 113160
- [7] Bouhaik I S, Meliani M H, Suleiman R K and Saleh T A 2023 Mechanistic insights into acid orange 7 azo dye (AO7) reduction using DFT calculations *Polyhedron* **245** 116648
- [8] Van Hung N, Nguyet B T M, Nghi N H, Nguyen V T, Binh T V, Tu N T T, Dung N N and Khieu D Q 2021 Visible light photocatalytic degradation of organic dyes using W-modified TiO<sub>2</sub>/SiO<sub>2</sub> catalyst *Vietnam Journal of Chemistry* **59** 620–38
- [9] Valli Nachiyar C, Rakshi A D, Sandhya S, Britlin Deva Jebasta N and Nellore J 2023 Developments in treatment technologies of dye-containing effluent: a review *Case Studies in Chemical and Environmental Engineering* **7** 100339
- [10] Xie K, Fang J, Li L, Deng J and Chen F 2022 Progress of graphite carbon nitride with different dimensions in the photocatalytic degradation of dyes: a review *J. Alloys Compd.* **901** 163589
- [11] Zhang H, Liu Y, Liu H, Yin J, Shi L and Tang H 2023 Surface anchoring of nickel sulfide clusters as active sites and cocatalysts for photocatalytic antibiotic degradation and bacterial inactivation *J. Colloid Interface Sci.* **637** 421–30
- [12] Hong J, Cho K-H, Presser V and Su X 2022 Recent advances in wastewater treatment using semiconductor photocatalysts *Current Opinion in Green and Sustainable Chemistry* **36** 100644
- [13] Wang S, Xia Y, Yan G, Chen M, Wang X, Wu L and Liang R 2022 PDI bridged MIL-125(Ti)-NH<sub>2</sub> heterojunction with frustrated Lewis pairs: A promising photocatalyst for Cr(VI) reduction and antibacterial application *Appl. Catalysis B* **317** 121798
- [14] Zhang D, Hu H, Wei J-A, Xu X, Chen L, Wu X, Yu Q, Zhang B-X and Wang L 2023 Zr-doped TiO<sub>2</sub> ceramic nanofibrous membranes for enhancing photocatalytic organic pollutants degradation and antibacterial activity *Colloids Surf. A* **665** 131231
- [15] Amelia S R et al 2024 One pot synthesis and performance of N- and (Mg,B,N)-doped ZnO for photocatalytic and antibacterial applications: Experimental and theoretical investigations *Ceram. Int.* **50** 11216–35
- [16] Anusuya M, Nagaveni A, Jayanthi E, Leelavathi H, Yogeswari B, Poonkodi K, Vimaladevi K, Prabhu V and Velayutham Pillai M 2024 Green-synthesized flattened rice-shaped CuO and metal doped CuO nanoparticles using Bauhinia racemosa Lam. leaves extract and their photocatalytic and biological applications *Inorg. Chem. Commun.* **162** 112289
- [17] Hwang I-S, Mahadik M A, Song M S, Lee S-W, Oh B-T, Lee H H, Chae W-S, Choi S H and Jang J S 2023 Influence of ultrafast microwave deposition on morphology and growth mechanism of WO<sub>3</sub> nanosheet photoanode for efficient bacterial inactivation and decomposition of organic pollutants *J. Environ. Chem. Eng.* **11** 109985
- [18] Yang H, He D, Liu C, Zhang T, Qu J, Jin D, Zhang K, Lv Y, Zhang Z and Zhang Y N 2022 Visible-light-driven photocatalytic disinfection by S-scheme alpha-Fe<sub>2</sub>O<sub>3</sub>/g-C<sub>3</sub>N<sub>4</sub> heterojunction: Bactericidal performance and mechanism insight *Chemosphere* **287** 132072
- [19] Passi M and Pal B 2024 A novel ternary Fe(III)-SrTiO<sub>3</sub>-GO nanocomposite for LED-light-driven photocatalytic degradation of norfloxacin antibiotic: Performance, mineralization ability, degradation pathway, and mechanistic insight *Chem. Eng. J.* **479** 147685
- [20] Song M S, Patil R P, Hwang I S, Mahadik M A, Jang T H, Oh B T, Chae W S, Choi S H, Lee H H and Jang J S 2023 *In situ* fabrication of Ag decorated porous ZnO photocatalyst via inorganic-organic hybrid transformation for degradation of organic pollutant and bacterial inactivation *Chemosphere* **341** 140057
- [21] Hassan M M, Khan W, Azam A and Naqvi A H 2014 Effect of size reduction on structural and optical properties of ZnO matrix due to successive doping of Fe ions *J. Lumin.* **145** 160–6
- [22] Ravichandran A T, Catherine Siriya Pushpa K, Ravichandran K, Arun T, Ravidhas C and Muralidharan B 2016 Effect of size reduction on the magnetic and antibacterial properties of ZnO:Zr:Mn nanoparticles synthesized by a cost-effective chemical method *J. Mater. Sci., Mater. Electron.* **27** 5825–32

- [23] Ramos P G, Espinoza J, Sánchez L A and Rodriguez J 2023 Enhanced photocatalytic degradation of Rhodamine B employing transition metal (Fe, Cu, Co) doped ZnO/rGO nanostructures synthesized by electrospinning hydrothermal technique *J. Alloys Compd.* **966** 171559
- [24] Yakout S M and El-Sayed A M 2019 Enhanced ferromagnetic and photocatalytic properties in Mn or Fe doped p-CuO/n-ZnO nanocomposites *Adv. Powder Technol.* **30** 2841–50
- [25] Kayani Z N, Abbas E, Saddiqe Z, Riaz S and Naseem S 2018 Photocatalytic, antibacterial, optical and magnetic properties of Fe-doped ZnO nano-particles prepared by sol-gel *Mater. Sci. Semicond. Process.* **88** 109–19
- [26] Hui A, Ma J, Liu J, Bao Y and Zhang J 2017 Morphological evolution of Fe doped sea urchin-shaped ZnO nanoparticles with enhanced photocatalytic activity *J. Alloys Compd.* **696** 639–47
- [27] Liu Y and Yang X 2023 Effects of Fe doping on the magnetic and absorption spectrum of graphene-like ZnO monolayer from first-principles calculations *Chem. Phys.* **565** 111742
- [28] Rao Y B S et al 2023 Effect of Fe doped and capping agent—structural, optical, luminescence, and antibacterial activity of ZnO nanoparticles *Chemical Physics Impact* **7** 100270
- [29] Nadeem M S, Munawar T, Mukhtar F, Naveed ur Rahman M, Riaz M and Iqbal F 2021 Enhancement in the photocatalytic and antimicrobial properties of ZnO nanoparticles by structural variations and energy bandgap tuning through Fe and Co co-doping *Ceram. Int.* **47** 11109–21
- [30] Cai H, Zhang D, Ma X and Ma Z 2022 A novel ZnO/biochar composite catalysts for visible light degradation of metronidazole *Sep. Purif. Technol.* **288** 120633
- [31] Sutar S, Otari S and Jadhav J 2022 Biochar based photocatalyst for degradation of organic aqueous waste: a review *Chemosphere* **287** 132200
- [32] Rangarajan G, Jayaseelan A and Farnood R 2022 Photocatalytic reactive oxygen species generation and their mechanisms of action in pollutant removal with biochar supported photocatalysts: a review *J. Clean. Prod.* **346** 131155
- [33] An X, Wang H, Dong C, Jiang P, Wu Z and Yu B 2022 core-shell P-laden biochar/ZnO/g-C<sub>3</sub>N<sub>4</sub> composite for enhanced photocatalytic degradation of atrazine and improved P slow-release performance *J. Colloid Interface Sci.* **608** 2539–48
- [34] Xie X, Li S, Zhang H, Wang Z and Huang H 2019 Promoting charge separation of biochar-based Zn-TiO<sub>2</sub>/pBC in the presence of ZnO for efficient sulfamethoxazole photodegradation under visible light irradiation *Sci. Total Environ.* **659** 529–39
- [35] Xia Q, Zhang L, Zhan P, Tong Z, Qing Y, He J, Wu Z, Wang H, Shao L and Liu N 2024 Combination of microwave with acid deep eutectic solvent pretreatment for reed (*Phragmites australis*) fractionation *Renewable Energy* **225** 120286
- [36] Chen M, Bao C, Hu D, Jin X and Huang Q 2019 Facile and low-cost fabrication of ZnO/biochar nanocomposites from jute fibers for efficient and stable photodegradation of methylene blue dye *J. Anal. Appl. Pyrolysis* **139** 319–32
- [37] Alves Z, Ferreira N M, Figueiredo G, Mendo S, Nunes C and Ferreira P 2022 Electrically conductive and antimicrobial agro-food waste biochar functionalized with zinc oxide particles *Int. J. Mol. Sci.* **23** 8022
- [38] Cho S H et al 2023 Applications of agricultural residue biochars to removal of toxic gases emitted from chemical plants: a review *Sci. Total Environ.* **868** 161655
- [39] Nguyen B T M, Nghi N H, Tien N A, Khieu D Q, Duc H D and Hung N V 2022 Enhanced adsorption of methylene blue by chemically modified materials derived from *Phragmites australis* stems *Acta Chimica Slovenica* **69** 811–25
- [40] Mancuso A, Sacco O, Sannino D, Pragliola S and Vaiano V 2020 Enhanced visible-light-driven photodegradation of Acid Orange 7 azo dye in aqueous solution using Fe-N co-doped TiO<sub>2</sub> *Arabian J. Chem.* **13** 8347–60
- [41] Yosefi L, Haghighi M and Margan P 2022 Novel flowerlike nanoheterojunction design of p-BiOBr-p-NiO photocatalyst with enhanced photocatalytic activity for degradation of acid orange 7 and methylene blue *Materials Today Sustainability* **19** 100173
- [42] Arumugam S, Bavani T, Preeyanghaa M, Alaswad S O, Neppolian B, Madhavan J and Murugesan S 2022 A facile synthesis of visible light driven Ni<sub>3</sub>V<sub>2</sub>O<sub>8</sub> nano-cube/BiVO<sub>4</sub> nanorod composite photocatalyst with enhanced photocatalytic activity towards degradation of acid orange 7 *Chemosphere* **308** 136100
- [43] Jiang X, Zhang B, Liu B, Tang X and Tang L 2019 Experimental and theoretical study of visible light driven scandium (III) doped ZnO for antibacterial activity *Ceram. Int.* **45** 19948–55
- [44] He Y, Wang Y, Hu J, Wang K, Zhai Y, Chen Y, Duan Y, Wang Y and Zhang W 2021 Photocatalytic property correlated with microstructural evolution of the biochar/ZnO composites *Journal of Materials Research and Technology* **11** 1308–21
- [45] Shine K P and Perry G E 2023 Radiative forcing due to carbon dioxide decomposed into its component vibrational bands† *Q. J. R. Meteorolog. Soc.* **149** 1856–66
- [46] Prabhu S, Pudukudy M, Harish S, Navaneethan M, Sohila S, Murugesan K and Ramesh R 2020 Facile construction of djembe-like ZnO and its composite with g-C<sub>3</sub>N<sub>4</sub> as a visible-light-driven heterojunction photocatalyst for the degradation of organic dyes *Mater. Sci. Semicond. Process.* **106** 104754
- [47] Pi L, Jiang R, Zhou W, Zhu H, Xiao W, Wang D and Mao X 2015 g-C<sub>3</sub>N<sub>4</sub> modified biochar as an adsorptive and photocatalytic material for decontamination of aqueous organic pollutants *Appl. Surf. Sci.* **358** 231–9
- [48] Li Y and Liu X 2014 Activated carbon/ZnO composites prepared using hydrochars as intermediate and their electrochemical performance in supercapacitor *Mater. Chem. Phys.* **148** 380–6
- [49] Hu H, Sun L, Gao Y, Wang T, Huang Y, Lv C, Zhang Y F, Huang Q, Chen X and Wu H 2020 Synthesis of ZnO nanoparticle-anchored biochar composites for the selective removal of perchlorate, a surrogate for perchlorate, from radioactive effluents *J. Hazard. Mater.* **387** 121670
- [50] Jafari M, Rahimi M R, Ghaedi M, Javadian H and Asfaram A 2017 Fixed-bed column performances of azure-II and auramine-O adsorption by Pinus eldarica stalks activated carbon and its composite with zno nanoparticles: optimization by response surface methodology based on central composite design *J. Colloid Interface Sci.* **507** 172–89
- [51] Gonullu M P, Cakil D D and Cetinkaya C 2024 Influence of thermal treatment and Fe doping on ZnO films by ultrasonic spray pyrolysis *Thin Solid Films* **793** 140265
- [52] Gholami P, Dinpazhoh L, Khataee A and Orooji Y 2019 Sonocatalytic activity of biochar-supported ZnO nanorods in degradation of gemifloxacin: Synergy study, effect of parameters and phytotoxicity evaluation *Ultrason. Sonochem.* **55** 44–56
- [53] Wang S, Zhou Y, Han S, Wang N, Yin W, Yin X, Gao B, Wang X and Wang J 2018 Carboxymethyl cellulose stabilized ZnO/biochar nanocomposites: Enhanced adsorption and inhibited photocatalytic degradation of methylene blue *Chemosphere* **197** 20–5
- [54] Saadi H, Rhouma F I H, Benzarti Z, Bougrioua Z, Guermazi S and Khirouni K 2020 Electrical conductivity improvement of Fe doped ZnO nanopowders *Mater. Res. Bull.* **129** 110884
- [55] Jenish S L, Valanarasu S, Prakash B, Veerathamang K, Vinoth S, Al-Enizi A M, Ubaidullah M, Reddy V R M and Karim A 2022 Improved optical and electrical properties of Fe doped ZnO nanostructures facily deposited by low-cost SILAR method for photosensor applications *Surfaces and Interfaces* **31** 102071

- [56] Jin Z, Wang A-J, Sun Y-R, Li J, Ma R and Ding Y 2024 High selectivity and sensitivity gas sensors to n-butanol based on Ni-doped ultrathin porous single-crystalline ZnO nanosheets *Sens. Actuators, A* **369** 115115
- [57] Kundu S, Sain S, Satpati B, Bhattacharyya S R and Pradhan S K 2015 Structural interpretation, growth mechanism and optical properties of ZnO nanorods synthesized by a simple wet chemical route *RSC Adv.* **5** 23101–13
- [58] Lavand A B and Malghe Y S 2015 Visible light photocatalytic degradation of 4-chlorophenol using C/ZnO/CdS nanocomposite *Journal of Saudi Chemical Society* **19** 471–8
- [59] Wu X, Wei Z, Zhang L, Wang X, Yang H and Jiang J 2014 Optical and magnetic properties of Fe Doped ZnO nanoparticles obtained by hydrothermal synthesis *J. Nanomater.* **2014** 1–6
- [60] Ghosh A and Choudhary R N P 2009 Structural evolution and visible photoluminescence of Zn–ZnO nanophosphor *Physica Status Solidi(A)* **206** 535–9
- [61] Das J, Mishra D K, Srinivasu V V, Sahu D R and Roul B K 2015 Photoluminescence and Raman studies for the confirmation of oxygen vacancies to induce ferromagnetism in Fe doped Mn:ZnO compound *J. Magn. Magn. Mater.* **382** 111–6
- [62] Liang S, An M, Xia S, Zhang B, Xue B and Xu G 2023 Enhanced photocatalytic degradation of methyl orange by TiO<sub>2</sub>/biochar composites under simulated sunlight irradiation *Opt. Mater.* **142** 114105
- [63] Mishra D K, Samad S K, Varma A K and Mendhe V A 2018 Pore geometrical complexity and fractal facets of Permian shales and coals from Auranga Basin, Jharkhand, India *J. Nat. Gas Sci. Eng.* **52** 25–43
- [64] Hussein E A and Kareem S H 2020 Magnetic mesoporous silica material (Fe<sub>3</sub>O<sub>4</sub>@mSiO<sub>2</sub>) as adsorbent and delivery system for ciprofloxacin drug *IOP Conf. Ser.: Mater. Sci. Eng.* **871** 012020
- [65] Peng X, Wang M, Dai H, Qiu F and Hu F 2020 *In situ* growth of carbon nitride on titanium dioxide/hemp stem biochar toward 2D heterostructured photocatalysts for highly photocatalytic activity *Environmental Science and Pollution Research* **27** 39198–210
- [66] Liu Q, Chen T, Guo Y, Zhang Z and Fang X 2016 Ultrathin g-C<sub>3</sub>N<sub>4</sub> nanosheets coupled with carbon nanodots as 2D/0D composites for efficient photocatalytic H<sub>2</sub> evolution *Appl. Catalysis B* **193** 248–58
- [67] Shan S, Lv Z and Wu H 2024 A novel readily recyclable Fe<sub>3</sub>O<sub>4</sub>/ZnO/loofah biochar composite for efficient degradation of organic pollutants under visible light *Mater. Sci. Eng. B* **303** 117272
- [68] Liu J, Zhou S, Gu P, Zhang T, Chen D, Li N, Xu Q and Lu J 2020 Conjugate Polymer-clothed TiO<sub>2</sub>@V<sub>2</sub>O<sub>5</sub> nanobelts and their enhanced visible light photocatalytic performance in water remediation *J. Colloid Interface Sci.* **578** 402–11
- [69] Berdini F, Otalvaro J O, Avena M and Brigante M 2022 Photodegradation of doxycycline in water induced by TiO<sub>2</sub>-MCM-41. Kinetics, TOC evolution and reusability *Results in Engineering* **16** 100765
- [70] Hsieh A-H, Wu K C W and Hsu C-C 2014 Kinetic study of Acid Orange 7 degradation using plasmas in NaNO<sub>3</sub> solution sustained by pulsed power *J. Taiwan Inst. Chem. Eng.* **45** 1558–63
- [71] Xu L, Zhao H, Shi S, Zhang G and Ni J 2008 Electrolytic treatment of C.I. Acid Orange 7 in aqueous solution using a three-dimensional electrode reactor *Dyes Pigm.* **77** 158–64
- [72] Muthirulan P, Devi C N and Sundaram M M 2014 TiO<sub>2</sub> wrapped graphene as a high performance photocatalyst for acid orange 7 dye degradation under solar/UV light irradiations *Ceram. Int.* **40** 5945–57
- [73] Lan W, Lin Z L and Kai G M 2017 Kinetics analysis of photocatalytic degradation of Acid Orange 7 by Co/N/Er<sup>3+</sup>: Y<sub>3</sub>Al<sub>5</sub>O<sub>12</sub>/TiO<sub>2</sub> films *Journal of Advanced Oxidation Technologies* **20** 20160185
- [74] Guan K, Zhou P, Zhang J and Zhu L 2020 Catalytic degradation of acid orange 7 in water by persulfate activated with CuFe<sub>2</sub>O<sub>4</sub>@RSDBC *Mater. Res. Express* **7** 016529
- [75] Han F, Kambala V S R, Dharmarajan R, Liu Y and Naidu R 2018 Photocatalytic degradation of azo dye acid orange 7 using different light sources over Fe<sup>3+</sup>-doped TiO<sub>2</sub> nanocatalysts *Environmental Technology & Innovation* **12** 27–42
- [76] Antoniadou M, Arfanis M K, Ibrahim I and Falaras P 2019 Bifunctional g-C<sub>3</sub>N<sub>4</sub>/WO<sub>3</sub> thin films for photocatalytic water purification *Water* **11** 2439
- [77] Swetha S, Abdel-Maksoud M A, Okla M K, Janani B, Dawoud T M, El-Tayeb M A and Sudheer Khan S 2023 Triple-mechanism driven Fe-doped n-n hetero-architecture of Pr<sub>6</sub>O<sub>11</sub>-MoO<sub>3</sub> decorated g-C<sub>3</sub>N<sub>4</sub> for doxycycline degradation and bacterial photoinactivation *Chem. Eng. J.* **461** 141806
- [78] Iqbal A, Saidu U, Sreekantan S, Ahmad M N, Rashid M, Ahmed N M, Danial W H and Wilson L D 2021 Mesoporous TiO<sub>2</sub> Implanted ZnO QDs for the photodegradation of tetracycline: Material design, structural characterization and photodegradation mechanism *Catalysts* **11** 1205